



Nd:YAG laser micro-welding of ultra-thin FeCo–V magnetic alloy: optimization of weld strength

H. MOSTAAN¹, M. SHAMANIAN², S. HASANI³, M. SAFARI⁴, J. A. SZPUNAR⁵

1. Department of Materials and Metallurgical Engineering, Faculty of Engineering,
Arak University, Arak 38156-8-8349, Iran;

2. Department of Materials Engineering, Isfahan University of Technology, Isfahan 84156-83111, Iran;

3. Department of Mining and Metallurgical Engineering, Yazd University, Yazd 89195-741, Iran;

4. Department of Mechanical Engineering, Arak University of Technology, Arak 3818141167, Iran;

5. Department of Mechanical Engineering, University of Saskatchewan, Saskatoon, SK S7N 5A9, Canada

Received 20 March 2016; accepted 13 September 2016

Abstract: The main aim of this research is to optimize the tensile strength of laser welded FeCo–V alloy. A mathematical relationship was developed to predict tensile strength of the laser beam welded FeCo–V foils by incorporating process parameters such as lamping current, welding speed, pulse duration and focused position. The procedure was established to improve the weld strength and increase the productivity. The results indicate that the pulse duration and welding speed have the greatest influence on tensile strength. The obtained results showed that the tensile strength of the weld joints increase as a function of increasing pulse duration reaching to a maximum at a pulse duration value of 2.25 ms. Moreover, the tensile strength of joints increases with decrease in welding speed reaching to a maximum at a welding speed of 125 mm/min. It has been shown that increase in pulse duration and decrease in welding speed result in increased effective peak power density and hence formation of more resistant welds. At higher pulse durations and lower welding speeds, the tensile strength of weld joints decreases because of formation of solidification microcracks in the fusion zone.

Key words: Nd:YAG laser welding; FeCo–V magnetic alloys; response surface methodology; mechanical properties; optimization

1 Introduction

FeCo-based alloys have attracted considerable attention due to their excellent soft magnetic properties as well as high Curie temperature, high saturation induction and low magnetic core loss [1–3]. For high performance applications in many fields such as rotor or stator laminations in motors for power generation, such magnetic materials are required to possess not only the abovementioned magnetic properties but also good mechanical properties, such as high strength and ductility [4,5]. During the past few years a considerable amount of research has been devoted to these alloys in order to develop optimum magnetic and mechanical properties for application in modern aircraft generators. However, binary Fe–Co alloys remained without industrial applications, mainly because of its extreme brittleness. It has been discovered that the addition of vanadium to

those alloys can have beneficial effects on the ductility and strength without serious degradation of the magnetic properties [6]. These magnetic alloys with 50%–52% Co and 5%–13% V revealed in the first half of the 20th century, which are called “vicalloy” [7], belong to the group of magnetically hard materials. Depending on the amount of vanadium, the coercive force of the alloys varies at 4.0–24.0 kA/m, the residual induction is between 1.25 and 0.6 T [8]. A distinguishing feature of FeCo–V alloys is their high plasticity, which enable us to obtain the above indicated magnetic properties in metallic ribbons up to 50 μm in thickness. This fact, along with the high temperature stability of magnetic characteristics, makes them suitable for some applications such as active parts of rotors of synchronous hysteresis motors (SHM) [8]. In order to deploy these magnetic alloys in SHMs, it is necessary to produce them in the form of ultra-thin foils. This requirement has been raised with the goal of obtaining increasingly denser and

smaller structures and devices and to minimize eddy current losses [9,10]. So, welding of these ultra-thin alloys is very crucial since uncontrolled welding parameters result in unexpected weld joint quality. On the other hand, FeCo–V alloys experience various phase transformations during heating-cooling cycles. These transformations are an ordering transformation in which disordered structure changes to ordered structure below a critical temperature ($T_c \sim 730$ °C) [11], an allotropic transformation in which ferrite phase with BCC (base-centered-cubic) structure transforms to austenite phase with FCC (face-centered-cubic) structure [12] and finally precipitation of vanadium rich- γ_2 phase (Co_3V) [13]. During welding of FeCo–V alloys, these phase transformations will occur which extremely influence the mechanical and magnetic properties. Therefore, it is of great importance to choose an appropriate welding process for joining of these alloys and to control process parameter to obtain a joint with desirable quality. Resistance and arc welding techniques are no longer suited for joining very thin metallic parts because these processes cause excessive melting, unacceptable heat affected zones (HAZs), and large distortion. Among various welding processes, laser beam welding has been chosen for joining the ultra-thin foils in the aforementioned industries because of its accuracy, precision, repeatability, low distortion and ability to produce good-strength welds [14]. These advantages came from its high power density, which make laser beam welding one of the key welding processes [15]. To achieve good weld quality, the combination of the output power, welding speed, focal position, shielding gas and position accuracy should be correctly selected [16]. In welding process, the input parameters influence the mechanical properties of the welded joints. Various optimization methods can be applied to defining the desired output variables through the development of mathematical models to specify the relationship between the input parameters and output variables. One of the most widely used methods to solve this problem is the

response surface methodology (RSM), in which the experimenter tries to approximate the unknown mechanism with an appropriate empirical model [17].

However, there is no information available in the open literature on prediction of optimum laser beam welding process parameters to attain the maximum tensile strength in FeCo–V alloy joints. The authors believe that the optimization of laser welding of FeCo–V foils using statistical approaches is considered as one of the essential objectives in production of SHMs industry since there are no sufficient data found in the literature. In the present work, firstly changes of mechanical properties during laser welding process will be discussed. Also, this research work aims to statistically optimize the laser welding of FeCo–V foils using RSM to achieve good weld bead quality with the maximum mechanical properties.

The authors believe that the findings of this research work would help with exploiting full advantages of FeCo–V alloys in the aforementioned applications.

This research work is the extension of our previous work in which the focus was on the fracture mechanic and fractographic study of the laser welded joints [18]. In this research work, the welding process has been done by a different laser welding machine and the obtained results in this work are not comparable with the previous published results.

2 Experimental

2.1 Material

The workpiece used was a 0.05 mm-thick FeCo–V magnetic alloy with the following chemical compositions (mass fraction, %): 7 V, 0.17 Mn, 43.25 Fe, and Co balance.

2.2 Laser welding process

A special fixture was used to hold the foils of FeCo–V alloy, as shown in Fig. 1. Foils with dimensions of 0.05 mm × 1000 mm × 25 mm are tightly rolled up

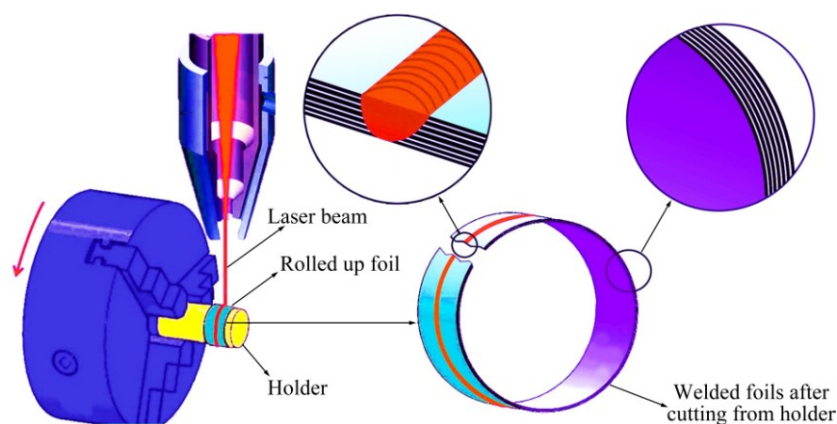


Fig. 1 Schematic illustration of laser welding set-up

around the holder. The control of the gap size during welding was crucial.

Then, the end of foil is fixed by glue to prevent any gap between the foils and to minimize the weld distortion. The holder begins to rotate and simultaneously the laser beam irradiates the center of specimen surface under the constant welding conditions as shown in Table 1. The diameter of holder was 45.85 mm and so the circumference of the holder is about 140 mm. Regarding the dimensions of holder, by rolling up 1000 mm of foil around the holder, 7 turns of foil are placed around the holder. Therefore, depending on the laser beam parameters (heat input), a minimum of 2 foil layers or a maximum of 7 foil layers have been welded to each other. In other words, at the minimum heat input 2 foil layers and at the maximum heat input 7 foil layers were welded to each other.

Table 1 Laser welding parameters used in this study

Pulse shape	Focal length/mm	Beam spot size/mm	Pulse repetition rate/Hz	Laser light wavelength/nm
Rectangular	100	0.18	40	1064

A pulsed Nd:YAG laser with a maximum mean laser power of 800 W was used. Square shape pulses are the standard output of this laser. The available range for the laser parameters were: 1–1000 Hz for pulse frequency, 0.2–20 ms for pulse duration, and 0–40 J for pulse energy. A translational XYZ controllable table was used to move the fixture with an accurate speed under laser nozzle with 0.05 mm positioning precision. Pure argon gas with a flow rate of 15 L/min was used as shielding gas commonly on top of the weld through a particular design. Welding tests were carried out according to the design matrix in a random order to avoid any systematic error in the experiment.

2.3 Evaluations of mechanical properties

Uniaxial tensile testing was used to evaluate the tensile properties of the base metal using ASTM E8–04 while the standard ultimate tensile strength of the welds was determined using transverse samples cut from the welds by WEDM process according to Fig. 2.

The crosshead speed was constant in all tensile testing and equal to 0.5 mm/min. In order to ensure repeatability of tensile strength data, three samples for each condition were tested. These repetitions were performed for each point of the plan and the reported values in Tables 2 and 3 are mean values of these three values. The mechanical properties of the base metal are listed in Table 2.

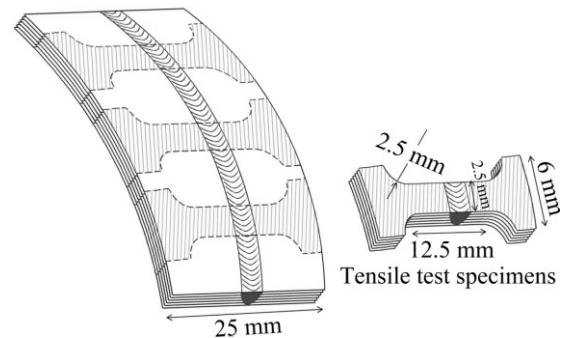


Fig. 2 Three-dimensional schematic diagram illustrating preparation of tensile test specimens

Table 2 Mechanical properties of studied material

Yield stress/MPa	Tensile stress/MPa	Elongation/%	Vickers hardness
1241	1562	3.3	740

Microhardness tests were also performed on workpieces. These tests were performed using a sclerometer (Wilson-Walpert) with magnification of 400. Used sclerometer is able to measure the microhardness in Vickers scale with a force exertion range of 10 to 1000 g. For the measurement of the Vickers microhardness, a load of 100 g was exerted on a cross section of the welds in order to obtain hardness.

2.4 Microstructural analysis

The microstructural analysis was also performed by optical microscopy (OM). Specimens with dimensions of 18 mm × 3 mm were cut from the weld joints for OM, and wet polished using SiC emery papers of up to 4000 grit, and then buff polished to a mirror finish using diamond paste. After polishing, they were etched for about 5 s at room temperature using an etchant with composition of 5% FeCl₃ + 100 mL distilled water. Hitachi SEM equipped with energy dispersive X-ray spectroscopy system (EDS) and electron backscattered diffractometer (EBSD) was used in structure analysis, phase and microtextural evolutions. The HKL CHANNEL5 software was used to perform EBSD data visualization and post processing.

2.5 Optimization procedure

The statistical package Minitab® V.16.2.4 was used to obtain the mathematical relationship in the form of linear and quadratic equations for the measured responses. The optimization part in this software searches for a combination of factor levels that simultaneously satisfy the requirements placed (i.e. optimization criteria) on the response and process input factors.

3 Results and discussion

3.1 Microstructure evolution and mechanical properties of weld joint

3.1.1 Microstructure evolution

Figure 3 shows the microstructure and weld cross section of a typical laser weld joint of ultra-thin FeCo–V alloy.

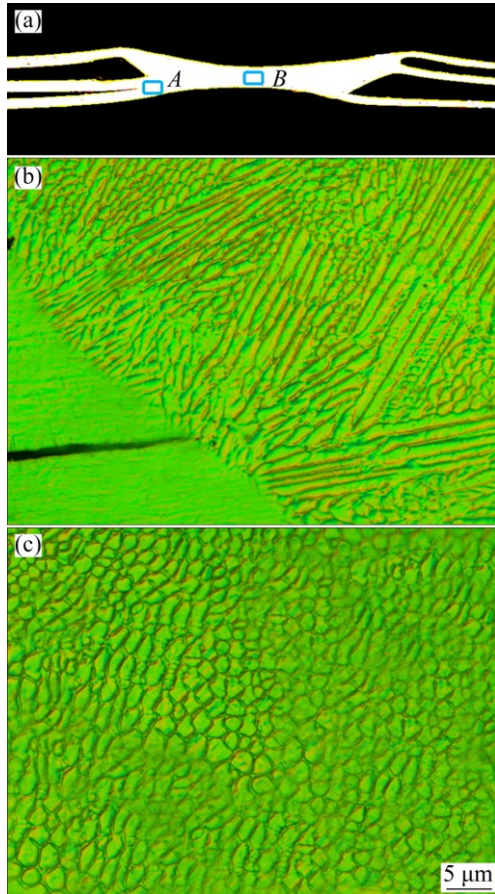


Fig. 3 Microstructures of weld cross section of typical laser weld joint: (a) Weld joint; (b) Region A; (c) Region B

It is evident that the fusion zone contained two different regions, namely cellular dendritic and equiaxed dendritic structure, as shown in Fig. 3. As shown, the direction of grains near the fusion line has obvious directional characteristics. In the weld pool crystallization, compared with spontaneous nucleation, nonspontaneous nucleation is dominant [19]. The energy barrier (ΔG) for the crystal to nucleate on the substrate is [20]

$$\Delta G = \frac{4\pi\gamma_{LC}^3 T_m^2}{3(\Delta H_m \Delta T)^2} (2 - 3\cos\theta + \cos^3\theta) \quad (1)$$

where γ_{LC} is the surface energy of the molten metal–solid interface, T_m is the equilibrium melting temperature, ΔH_m

is the latent heat of melting, ΔT is the undercooling below T_m and θ is the contact angle. If the molten metal can wet the base metal, the contact angle and consequently ΔG are zero. During laser welding of FeCo–V foil, the existing base metal grains at the fusion line act as the substrate for nucleation. Since chemical composition of the molten metal in the fusion zone (FZ) and substrate are the same, the molten metal can wet the substrate grains, and the crystals nucleate from the molten metal upon the base metal without difficulties. Epitaxial growth of grains near fusion line is shown in Fig. 3(b). These cellular grains grew epitaxially from the interface and followed the easy-growth direction $\{100\}$ of the parent FeCo–V grains. The solidification mode across the fusion zone changed from cellular to equiaxed dendritic because of the increase in cooling rate from the weld zone interface toward the centerline. When the solidification front approaches the weld centerline, the growth rate reaches its maximum as the temperature gradient is at its minimum. Therefore, as can be seen in Fig. 3(c), very fine equiaxed grains ($\sim 2 \mu\text{m}$) are formed in the center of fusion zone.

3.1.2 Phase evolutions

Phase map analysis of base metal and weld area of a typical laser welded FeCo–V alloy (obtained from EBSD data) are shown in Fig. 4. In this figure, ferrite (α phase) and austenite (γ phase) have been depicted by red and blue colors, respectively. As can be seen, base metal is dual phase and consists of both ferrite and some austenite clusters. But, after laser welding, the weld area is single phase and γ phase has been eliminated from microstructure. It is worthy to consider phase evolution during laser welding of FeCo–V alloy. It has been found by other researchers that when FeCo–V alloys containing more than 7% vanadium are heated up to $\alpha+\gamma$ region of phase diagram, γ phase would be stable during normal cooling. For the occurrence of $\gamma \rightarrow \alpha$ phase transformation and finally elimination of γ phase, very rapid cooling or sufficient strain is needed. On one hand, cooling rate during laser welding is very high. On the other hand, during rapid cooling of very small molten metal formed by laser beam, relatively large strain is induced in the weld area. From the EBSD data, the Kernel average misorientation (KAM) which represents the average misorientation between a given point and its nearest neighbors belonging to the same grain (and thus associated with a misorientation less than 5°) has been used to evaluate and map the local plastic strain in the weld joint. Figure 5 shows the KAM maps in the base metal and in the weld area. It is clear that the deformation is more concentrated in the weld area than in the other parts of the weld joint.

It seems that this strain concentration in the weld area is another main reason which results in $\gamma \rightarrow \alpha$ phase

transformation and subsequently elimination of γ phase from the structure.

3.1.3 Microtexture analysis across weld joint

In the field of FeCo–V alloys, texture investigations are of great interest since the texture determines the magnetic anisotropy that is important for practical applications, for example, for appropriate magnetic properties. Most of the main orientations usually found after rolling and annealing in both phases (γ and α) can be grouped into two sections of the Euler space, namely $\varphi_2=0^\circ$ and 45° . These orientations are presented in Fig. 6 and characterized by the classical Miller indices $\{hkl\}$ (uvw), where $\{hkl\}$ and (uvw) are the indices of the rolling plane and direction, respectively.

The φ_2 sections for the two phases of the base metal and the laser weld area are shown in Fig. 7. For BCC metals, the important fibers are the α -fiber, ε -fiber and γ -fiber. In the α -fiber, the fiber axis $\langle 110 \rangle$ is parallel to the rolling direction that includes $\{001\}\langle 110 \rangle$, $\{112\}\langle 110 \rangle$ and $\{111\}\langle 110 \rangle$ components. In the γ -fiber, the fiber axis $\langle 111 \rangle$ is parallel to the normal direction that includes $\{111\}\langle 110 \rangle$ and $\{111\}\langle 112 \rangle$ components. As can be seen in the $\varphi_2=45^\circ$ section (Fig. 7(a)), dominant α -fiber and relatively weak γ -fiber are present. Also, rotated cube texture component can be observed in the section of $\varphi_2=0^\circ$. But, after laser welding, α -fiber has been diminished and copper texture component has been formed in the structure. Diminishment of α -fiber during

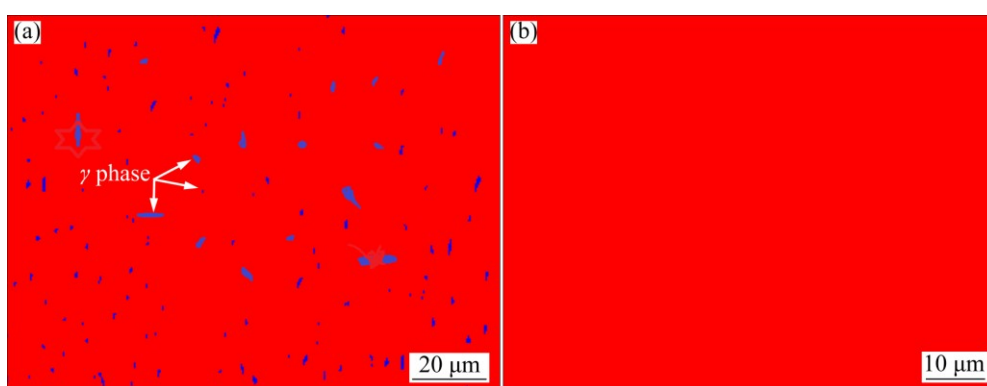


Fig. 4 Phase maps (obtained from EBSD data) from base metal (a) and center of weld area (b)

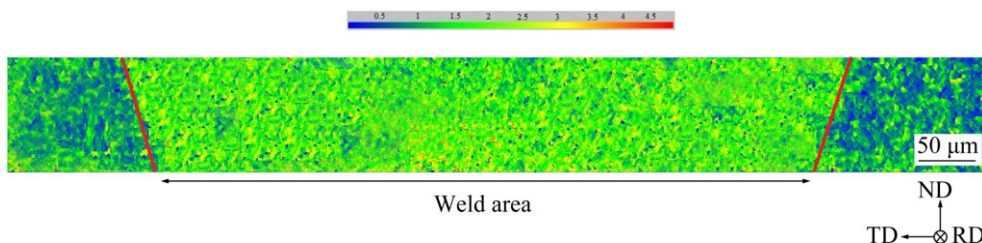


Fig. 5 KAM maps measured in different parts of weld joint

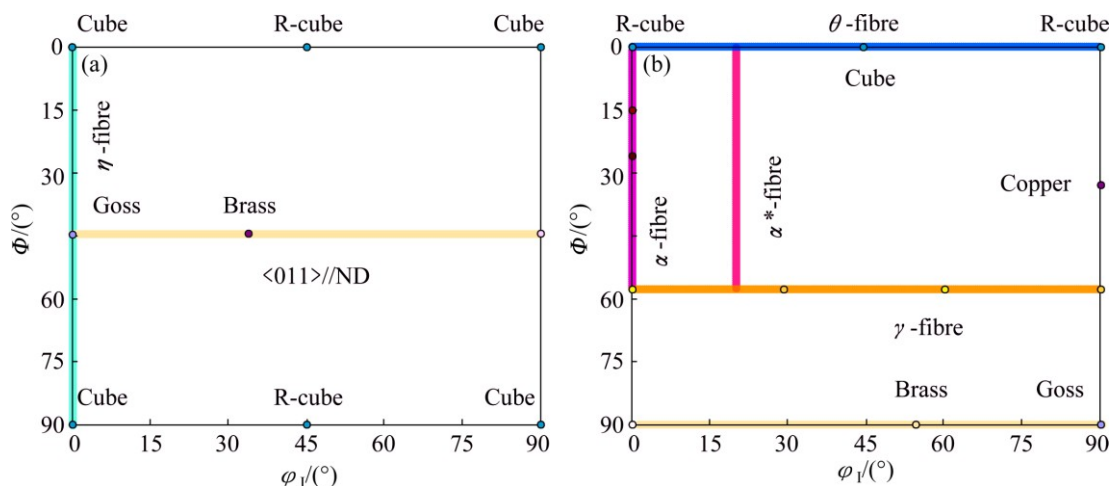


Fig. 6 Main orientations and fibers observed in BCC metal: (a) $\varphi_2=0^\circ$, orientation distribution function (ODF) section; (b) $\varphi_2=45^\circ$, ODF section

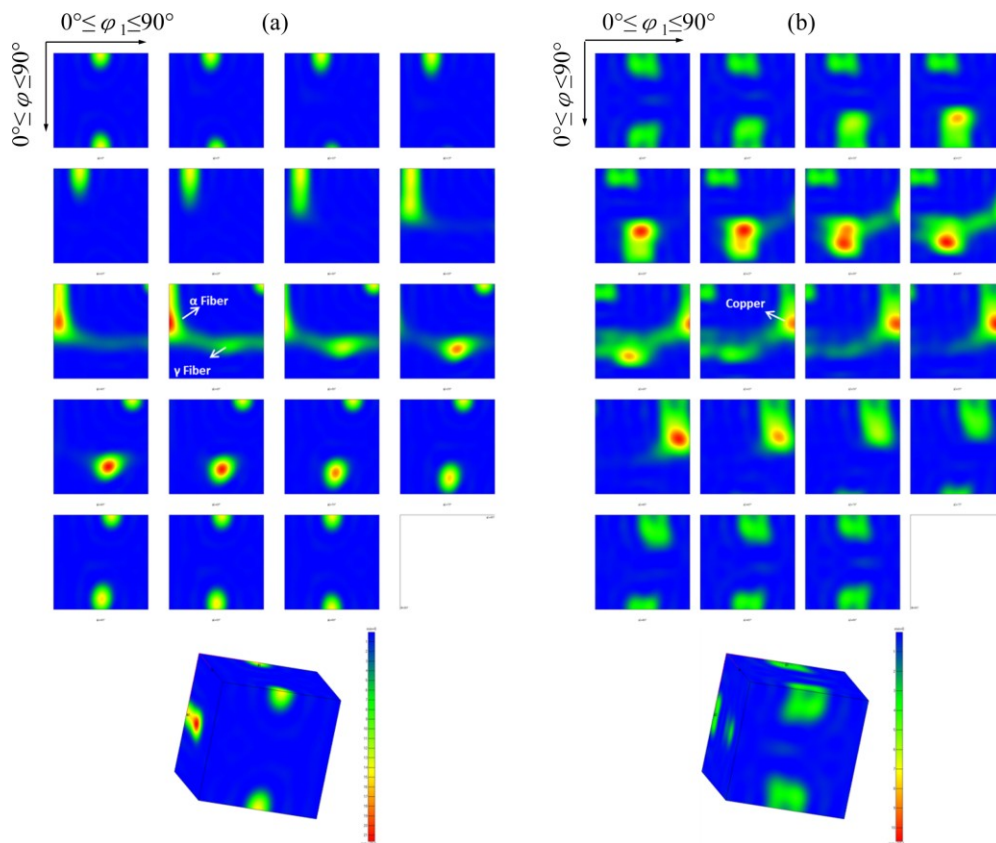


Fig. 7 Constant φ_2 sections of orientation distribution function in Euler space for base metal (a) and weld area (b)

laser welding of FeCo–V alloy leads to considerable changes in magnetic properties, for example severe reduction in residual induction [21].

3.1.4 Mechanical properties

Figure 8 shows the micro-hardness of a typical FeCo–V welded joint at various points at laser welding current of 145 A, welding speed of 125 mm/min, pulse duration of 2.25 ms and focused position of -1.25 mm.

It is seen that the hardness values in the heat affected zone (HAZ) and FZ are lower than that of BM. The mechanism of reduction of hardness in the HAZ and FZ were discussed in our previous work [18]. Decrease in hardness of HAZ and FZ is essentially due to the disordering transformation in these regions. As discussed earlier, despite lower hardness of HAZ, all the welded joints fracture in the FZ due to the higher stress concentration in this region (see Fig. 9).

3.2 Mathematical modeling by response surface methodology

Important parameters that influence the mechanical properties of laser welded joints were identified from literature and our laboratory experiments [22–25]. They are lamping current (I), pulse duration (T_p), welding speed (S) and focused position (F). In fact, the combinations of these parameters will mainly determine

the temperature distribution of the laser welded samples. Different combinations of welding parameters were used to carry out the trial runs in order to find out feasible working limits of electron beam welding parameters. A large number of trials have been conducted by variation of one of the process parameters and keeping the other constants. For instance, after gathering enough information about laser welding parameters of such thin foils from literature, in order to obtain the maximum level of lamping current or pulse duration, the level of welding speed was kept in its minimum value and vice versa. The working limit was determined after inspecting the weld beads for smooth and shiny appearance and the absence of any macro-defects such as cracks and porosity. The results obtained are as follows. If the lamping current is less than 130 A, there will be incomplete penetration. For lamping current greater than 160 A, foil tearing will be observed on the bead surface. If the pulse duration is lower than 1.5 ms, there will be a very rough and discontinuous weld bead appearance. For pulse duration greater than 3 ms, tearing of foils and large porosities will be observed due to the increased heat input. If the welding speed is lower than 50 mm/min, severe tearing of foils will be observed. For welding speed greater than 200 mm/min, there will be lack of fusion and lack of penetration. For the focused position

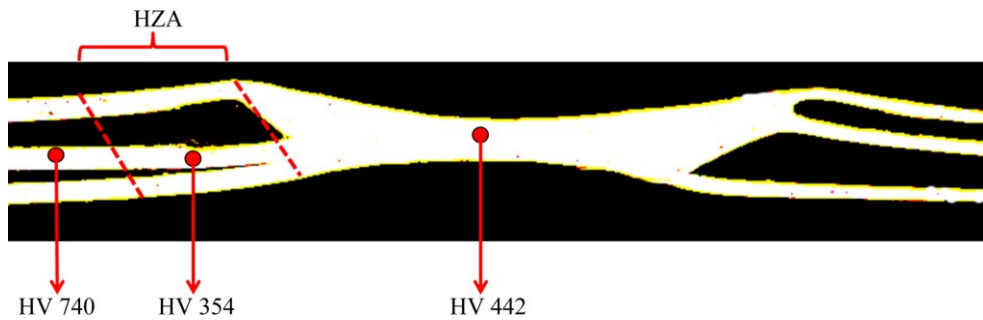


Fig. 8 Vickers-microhardness observed in weld cross section

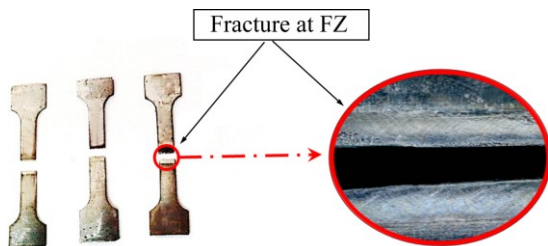


Fig. 9 View of weld joints after tensile test

higher than -0.5 mm, undercut will be observed on the weld bead surface and if the focused position is lower than -2 mm, spattering will occur. Focused position is defined by the distance between the focal point and the surface of the sheet. The focused position, which determines the spot size and consequently, the power density on the sheet surface, can also play an important role on weld bead dimension. The negative value of focused position denotes that the focused position (focal point) is placed under the foil surface. Considering the convenience of recording and processing experimental data, upper and lower levels of the parameters were coded as +2 and -2 , respectively.

The selected design matrix, shown in Table 3, is a central composite rotatable factorial design consisting of 31 sets of coded conditions [26]. It comprises a full replication of 24 factorial design plus seven center points and eight star points. In other words, in this matrix (Table 3), first 16 rows represent the full factorial ($2^4=16$) design and next eight rows show the star point and last seven rows exhibit the center point. All welding variables at the intermediate level (0) constitute the center points and the combinations of each of the welding variables at either its lowest (-2) level or highest (+2) level with the other three variables at the intermediate levels constitute the star points. Thus, the 31 experimental runs allowed the estimation of the linear, quadratic and two-way interactive effects of the laser welding parameters on the tensile strength.

For the selected input parameters, the second order polynomial regression equation used to represent the response surface is given by

Table 3 Design of experiment and response

No.	Factor				$\sigma_{F, LBW}/\text{MPa}$
	I	T_p	S	F	
1	-1	-1	-1	-1	776
2	1	-1	-1	-1	676
3	-1	1	-1	-1	596
4	1	1	-1	-1	632
5	-1	-1	1	-1	781
6	1	-1	1	-1	556
7	-1	1	1	-1	818
8	1	1	1	-1	698
9	-1	-1	-1	1	660
10	1	-1	-1	1	789
11	-1	1	-1	1	467
12	1	1	-1	1	719
13	-1	-1	1	1	759
14	1	-1	1	1	719
15	-1	1	1	1	773
16	1	1	1	1	857
17	-2	0	0	0	534
18	2	0	0	0	571
19	0	-2	0	0	700
20	0	2	0	0	654
21	0	0	-2	0	563
22	0	0	+2	0	758
23	0	0	0	-2	914
24	0	0	0	+2	948
25	0	0	0	0	996
26	0	0	0	0	1006
27	0	0	0	0	997
28	0	0	0	0	1003
29	0	0	0	0	995
30	0	0	0	0	1003
31	0	0	0	0	996

$$\sigma_F = f(I, T_p, S, F) \tag{2}$$

where σ_F is the tensile strength of laser welded joints.

Thus, the second order polynomial (regression) equation used to represent the response surface σ_F is

$$\sigma_F = \beta_0 + \sum_{i=1}^k \beta_i x_i + \sum_{i=1}^k \beta_{ii} x_i^2 + \sum_{i < j}^k \sum_{j=2}^k \beta_{ij} x_i x_j + \varepsilon \tag{3}$$

where β_0 is the response of the central point, the coefficient β_i is linear terms, the coefficient β_{ii} is the quadratic terms and the coefficient β_{ij} refers to the interaction terms. The ε measures the experimental errors. Usually, ε includes effects such as measurement error on the response, background noise and the effect of other variables. All the coefficients were calculated for their significance at 95% confidence level.

Accordingly, when the calculated value of P corresponding to a coefficient exceeds the standard tabulated value for the desired level of confidence (e.g. 5%), the coefficient becomes insignificant. The results of analysis of variance (ANOVA) for the response are given in Table 4.

According to the resulting ANOVA, the final mathematical model developed to predict the σ_F values of laser welded joints are given as

$$\sigma_F = 999.429 - 68.833T_p + 74.167S - 459.679I^2 - 275.679T_p^2 - 352.179S^2 - 119IS + 229IF + 184T_pS \tag{4}$$

The obtained data and the adequacy of the developed relationship were checked using the ANOVA. ANOVA test results for the developed model are presented in Table 5. The results of the ANOVA showed that the regression is significant with linear, quadratic and interaction terms for the developed model.

The normal probability plot of the residuals for tensile strength of laser welded joints is shown in Fig. 10 which reveals that the residuals are falling on the straight line. This means that the errors distributed normally. The

Table 4 ANOVA results for tensile strength

Term	Coefficient	SE coefficient	<i>T</i>	<i>P</i>
Constant	999.429	20.72	48.236	0.000
<i>I</i>	-4.833	22.38	-0.216	0.832
<i>T_p</i>	-68.833	22.38	-3.076	0.007
<i>S</i>	74.167	22.38	3.314	0.004
<i>F</i>	22.5	22.38	1.005	0.330
<i>I</i> × <i>I</i>	-459.679	41	-11.21	0.000
<i>T_p</i> × <i>T_p</i>	-275.679	41	-6.72	0.000
<i>S</i> × <i>S</i>	-352.179	41	-8.589	0.000
<i>F</i> × <i>F</i>	-64.179	41	-1.565	0.137
<i>I</i> × <i>T_p</i>	101.5	54.82	1.852	0.083
<i>I</i> × <i>S</i>	-119	54.82	-2.171	0.045
<i>I</i> × <i>F</i>	229	54.82	4.177	0.001
<i>T_p</i> × <i>S</i>	184	54.82	3.357	0.004
<i>T_p</i> × <i>F</i>	-52	54.82	-0.949	0.357
<i>S</i> × <i>F</i>	95.5	54.82	1.742	0.101

determination coefficient (R^2) indicates the goodness of fits for the model [17]. In this case, the value of the determination coefficient ($R^2=0.9436$) indicates that only less than 6% of the total variations are not explained by the model. All above considerations indicate the adequacy of the developed relationship.

3.3 Direct effects of individual process parameters on

σ_F

The main effects of different process variables on the σ_F , as predicted from the mathematical model, are illustrated in Fig. 11. It is evident from Fig. 11 that both the welding speed and the pulse duration have a strong effect on the tensile strength of laser welded joints.

In the case of the pulse duration and welding speed, the result demonstrates that increasing the pulse duration

Table 5 ANOVA test results for checking adequacy of proposed model

Source	DF	Seq SS	Adj SS	Adj MS	<i>F</i>	<i>P</i>	Significance
Regression	14	804155	804155	57440	19.11	0	√
Linear	4	1.64610	64610	16152	5.38	0.006	√
Square	4	616961	616961	154240	51.33	0	√
Interaction	6	122584	122584	20431	6.80	0.001	√
Residual error	16	48081	48081	3005			
Lack-of-fit	10	47963	47963	47963	496	0	√
Pure error	6	118	118	20			
Total	30	852236					
$R^2=94.36\%$							
Pred $R^2=76.56\%$							
Adj $R^2=89.42\%$							

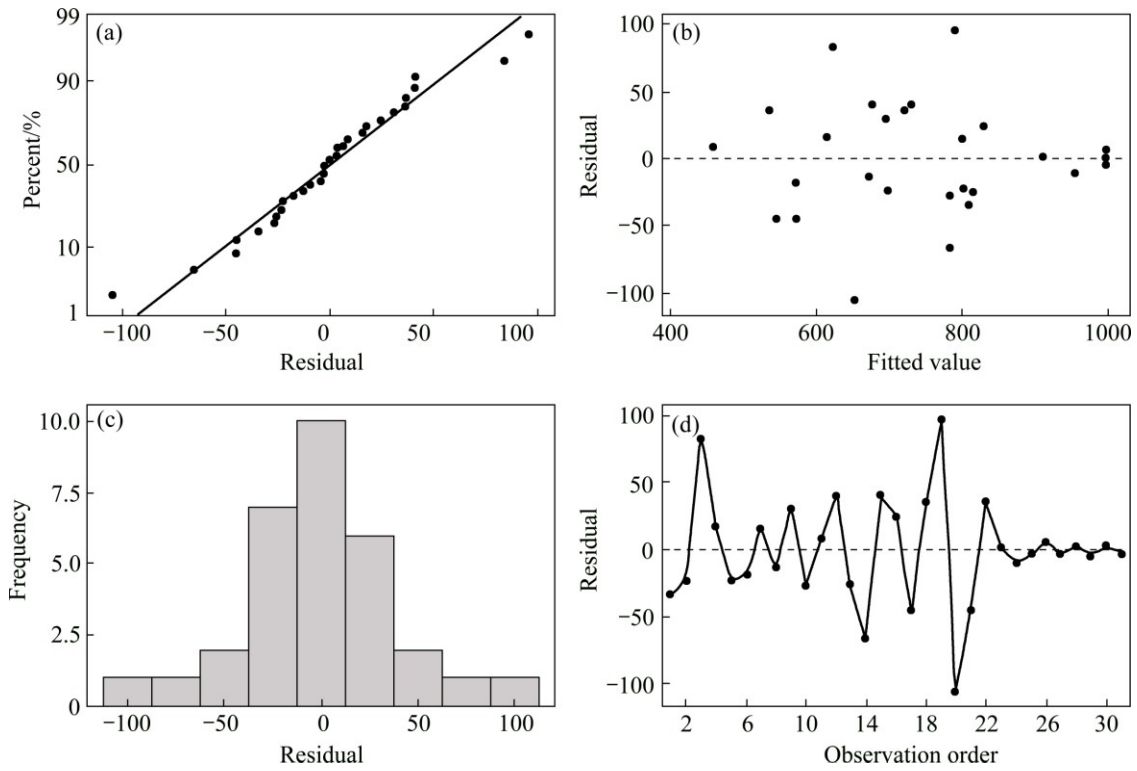


Fig. 10 Normal probability plots of tensile strength (σ_F): (a) Normal probability plot; (b) Versus fits; (c) Histogram; (d) Versus order

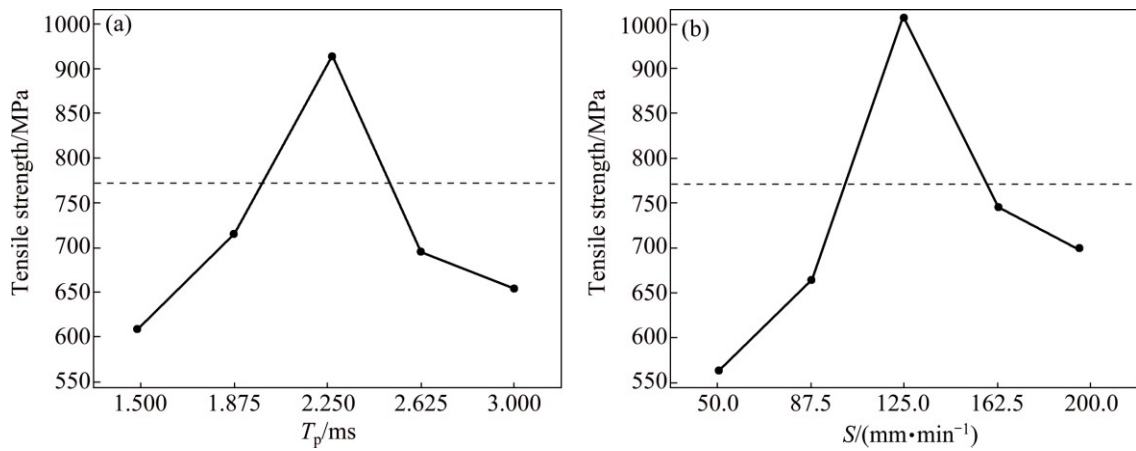


Fig. 11 Plots of main effects on σ_F response: (a) Pulse duration; (b) Welding speed

and welding speed until they reach their center value would result in improving the tensile strength, the tensile strength then starts to drop as the pulse duration and welding speed tend to increase above the center limit. Such behavior could be attributable to the following reasons. A continuous seam weld produced by a Nd:YAG pulsed laser welding process is a series of overlapping spot welds, as shown schematically in Fig. 12. The formation and the quality of the welds depend on the set-up of the various process parameters. To express the relationship of the overlap theory, relevant equations are formulated as follows.

If S is the travel speed, W is the minor diameter of

the spot weld, a is the major diameter of spot weld formed from a laser spot plus movement during a pulse, and b is the length in a single spot not overlapped by successive welding spots, and assuming one-dimensional overlapping, the percentage of overlap would be [25]

$$f = \left[1 - \frac{ST_F}{W + ST_p} \right] \times 100\% \tag{5}$$

In order to explain the behavior of pulsed laser weld joint, it is needed to define cumulative factor in order to take into account the contribution of the set of pulses hitting the area of a spot. For this, an effective peak power density (EPPD, d) is defined by

$$d = \frac{P_p}{A} \tag{6}$$

where P_p is the peak power; F is the cumulative overlapping index and A is the spot area of the beam. The F index is calculated by

$$F = 1 + n \left[1 - \frac{(n+1)S}{2Wf} \right]; n = \frac{Wf}{S} \tag{7}$$

where f is the pulse frequency. The values of effective peak power density of the weld series with different pulse durations and welding speeds are given in Table 6.

The results shown in Table 6 indicate that at higher levels of EPPDs, the values of tensile strength are higher.

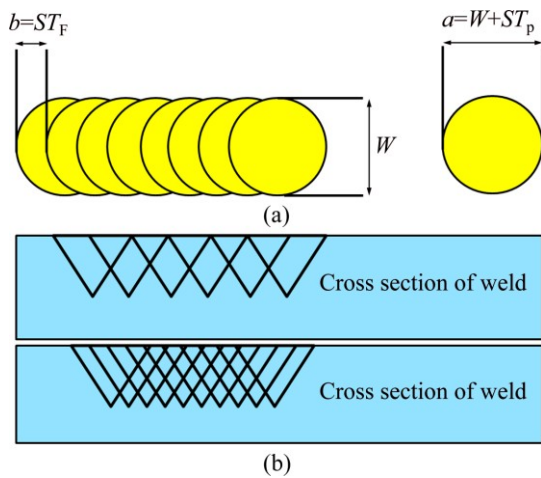


Fig. 12 Schematic diagram of rectangular laser power pulse trains and their corresponding partially overlapping spot welds (T_F is the pulse-to-pulse duration): (a) A series of overlapping spot welds forming a seam (Top view); (b) Continuous penetration profile

Increasing the EPPD increases overlapping of the successive pulses [24] which cause the pulsed process to be converted to a continuous mode and hence a well-founded weld joint is produced. As can be seen in Fig. 11, the tensile strength of the weld joints increases as a function of increasing pulse duration reaching a maximum at a pulse duration of 2.25 ms. As said above, the tensile strength increase is related to the increased EPPD which results in forming a more cohesive weld joint. Longer pulse duration causes a drop in the joint tensile strength and quality. This drop is due to very high heat input and consequently formation of large weld pool, bubble formation and large cavities, undercutting and solidification cracks formation at the joint along its length which may weaken the joint strength. Examples of weld defects which formed at high pulse duration values on the joint surface are shown in Fig. 13. Formation of these defects leads to severe decrease in tensile strength of weld joints. These micrographs are taken from surfaces of weld joints.

On the other hand, the tensile strength of joints increases by decrease in welding speed reaching a maximum at a welding speed of 125 mm/min. Similar to

Table 6 EPPD values in various pulse durations and welding speeds

Pulse duration/ms	EPPD/ ($W \cdot mm^{-2}$)	Welding speed/ ($mm \cdot min^{-1}$)	EPPD
1.500	7.48	50.0	12.58
1.875	8.78	87.5	11.34
2.250	10.22	125	10.22
2.625	11.33	162.5	8.45
3.000	12.53	200.1	7.66

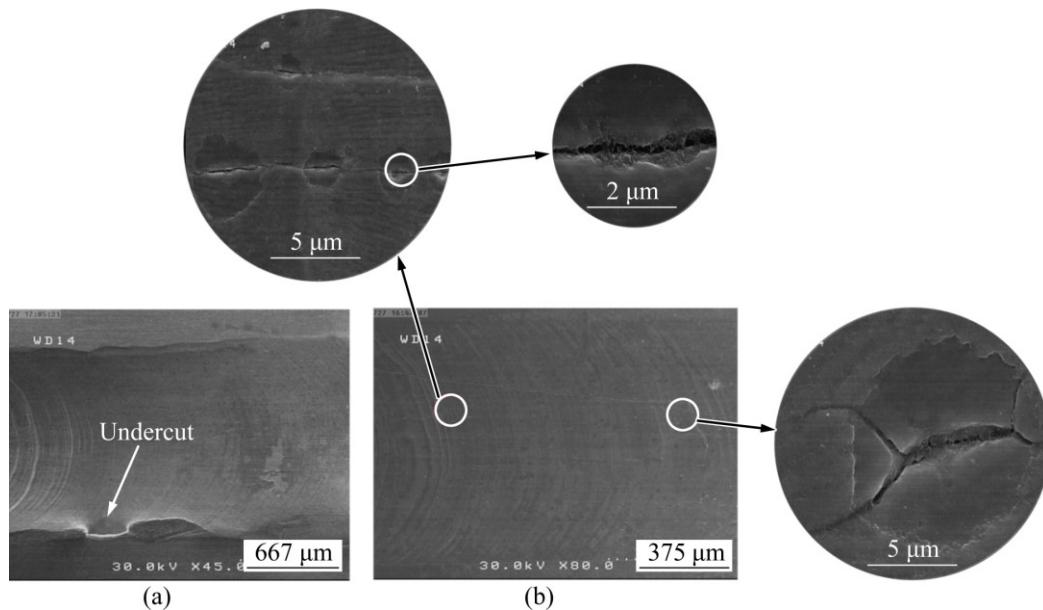


Fig. 13 Weld defects formation at high pulse duration: (a) Undercut; (b) Crack

effect of increase in pulse duration on the tensile strength, decrease in welding speed results in increased EPPD and hence forming a more resistant weld. From EPPD point of view, further decrease in welding speed gives better results for the joint strength but they are not preferable due to high operating costs, large deformation and large weld pool formation. In this conditions, formation of weld defects such as solidification cracks is more probable which can lead to decrease in joint strength. Formation of solidification cracks at very low welding speeds is shown in Fig. 14. These cracks are the main reasons for decrease in tensile strength at low welding speed.

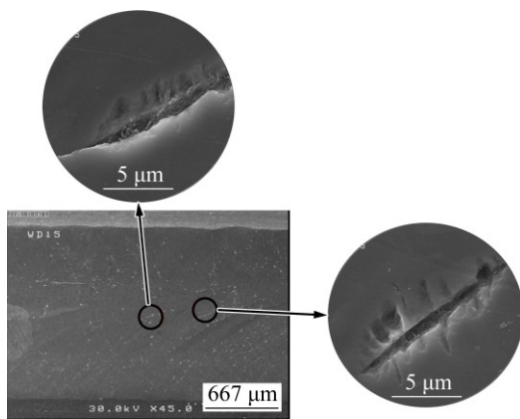


Fig. 14 Crack formation at very low welding speeds

3.4 Interaction effect of pulse duration and welding speed

Contour plots show a distinctive circular mound shape indicative of possible independence of factors with response. A contour plot was produced to visually display the region of optimal factor settings. For second-order response surfaces, such a plot can be more complex than the simple series of parallel lines that will occur with first-order models. By generating contour plots using software for response surface analysis, the optimum can be located with reasonable accuracy by characterizing the shape of the surface. If a contour patterning of circular shaped contours occurs, it tends to suggest independence of factor effects, while elliptical contours may indicate factor interactions. Response surface have been developed for the mathematical model, taking two parameters in the middle level and two parameters in the 'X' and 'Y' axes as well as the response in the 'Z' axis. Figures 15 shows the contour plots and 3D surface graphs of the interaction effects of welding speed and pulse duration on the σ_F . It should be noted that these plots are drawn when the two other parameters are in their middle values. In other words, this condition is the most prevalent which leads to better qualification interaction effect of the two welding parameters. As can be seen in this figure, the response

surface clearly indicates the optimal response point. The optimum tensile strength is exhibited by the apex of the response surfaces. From Fig. 15, it is also evident that tensile strength, σ_F has its maximum value, when the pulse duration and welding speed are in their middle values.

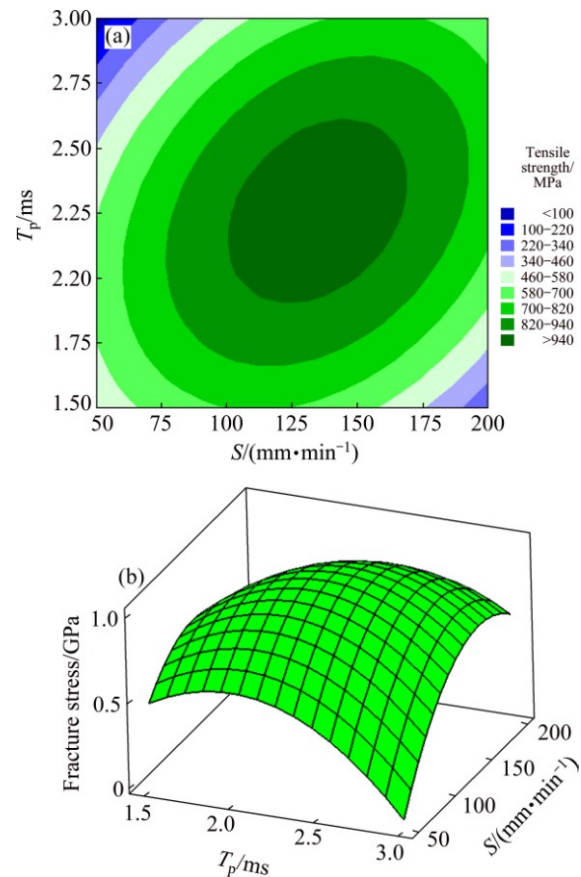


Fig. 15 Interaction effect of welding speed (a) and pulse duration (b) on σ_F value of welded samples ($I=145$ A, $F=-1.25$ mm)

4 Conclusions

Pulsed Nd:YAG laser welding of FeCo–V foils has been successfully conducted in this study. It was revealed that the hardness of HAZ and FZ decreased during laser welding and the entire samples fractured in the FZ. The RSM technique could be employed easily for developing mathematical model used in predicting the σ_F values of welded samples within the workable region of control parameters in the laser welding of ultra-thin foils. The main factors affected the tensile strength were the pulse duration and welding speed. To achieve high tensile strength of weld joint, pulse duration and welding speed must be set in their middle values, i. e., 2.25 ms and 125 mm/min, respectively. At higher pulse durations and lower welding speeds, the tensile strength of weld joints decreased because of the formation of solidification microcracks in the FZ.

References

- [1] WU L Z, CHEN J, DU Z Z, WANG J T. Microstructures of ultra-fine grained FeCoV alloys processed by ECAP plus cold rolling and their evolutions during tempering [J]. Transactions of Nonferrous Metals Society of China, 2010, 20(4): 602–606.
- [2] SUNDAR R S, DEEVI S C. Soft magnetic FeCo alloys: Alloy development, processing, and properties [J]. International Materials Reviews, 2013, 50(3): 157–192.
- [3] SOURMAIL T. Near equiatomic FeCo alloys: Constitution, mechanical and magnetic properties [J]. Progress in Materials Science, 2005, 50: 816–880.
- [4] SOURMAIL T. Evolution of strength and coercivity during annealing of FeCo based alloys [J]. Scripta Materialia, 2004, 51(6): 589–591.
- [5] SHAN Y, CHEN C, BI X. Role of precipitation in strength and ductility of FeCo–2V–Cr alloy with low coercivity [J]. Intermetallics, 2014, 54: 164–168.
- [6] WHITE J H, WAHL C V. Workable magnetic compositions containing principally iron and cobalt: US Patent, 1.862.559[P]. 1932.
- [7] BOZORTH R, NOSTRAND V. Ferromagnetism [M]. Moscow: Inostrannaya Literatura, 1993.
- [8] ZAKHAROV V M, LIBMAN M A, ESTRIN E I. On the role of atomic ordering in the formation of a high-coercivity state in iron-cobalt-vanadium alloys [J]. The Physics of Metals and Metallography, 2012, 113(1): 43–47.
- [9] ZHU F Z, BI X F, ZHANG S Q, GONG S K, XU H B. Phase transformation and magnetic properties of annealed Fe₅₂Co₄₆V_{1.8} alloy [J]. Vacuum, 2004, 75(1): 33–38.
- [10] DÍAZ-ORTIZ A, DRAUTZ R, FÄHNLE M. Structure and magnetism in bcc-based iron-cobalt alloys [J]. Physical Review B, 2006, 73(22): 224208-1–224208-15.
- [11] YU R H, BASU S, ZHANG Y, XIAO J Q. Magnetic domains and coercivity in FeCo soft magnetic alloys [J]. Journal of Applied Physics, 1999, 85(8): 6034–6036.
- [12] SUNDAR R, DEEVI S. Effect of heat-treatment on the room temperature ductility of an ordered intermetallic Fe–Co–V alloy [J]. Materials Science and Engineering A, 2004, 369(1–2): 164–169.
- [13] PINNELL M, MAHAJAN S, BENNETT J. Influence of thermal treatments on the mechanical properties of an Fe–Co–V alloy (remendur) [J]. Acta Metallurgica, 1976, 24: 1095–1106.
- [14] DUTTA MAJUMDAR J, MANNA I. Laser material processing [J]. International Materials Reviews, 2011, 56(5–6): 341–388.
- [15] LI K, LU F G, GUO S T, CUI H C, TANG X H. Porosity sensitivity of A356 Al alloy during fiber laser welding [J]. Transactions of Nonferrous Metals Society of China, 2015, 25(8): 2516–2523.
- [16] BLONDEAU R. Metallurgy and mechanics of welding [M]. New Jersey: John Wiley & Sons, 2013: 101.
- [17] MYERS R, MONTGOMERY D, ANDERSON-COOK C. Response surface methodology: Process and product optimization using designed experiments [M]. New Jersey: John Wiley & Sons, 2009.
- [18] MOSTAAN H, SHAMANIAN M, MONIRVAGHEFI S M, BEHJATI P, HASANI S, MOGHADDAM M F, AMIRI M, SZPUNAR J A. Analysis and characterization of microstructural evolutions, mechanical response and fracture mechanism of laser welded Fe–Co–V ultra-thin foils [J]. Optics & Laser Technology, 2015, 68: 211–219.
- [19] KOU S. Welding metallurgy [M]. 2nd ed. New Jersey: John Wiley & Sons, 2003.
- [20] PORTER D, EASTERLING M S K. Phase transformation in metals and alloys [M]. New York: CRC Press, 2001.
- [21] MOSTAAN H, SHAMANIAN M, MONIRVAGHEFI S M, BEHJATI P, SZPUNAR J A. Magnetic properties assessment of laser welded ultra-thin Fe–Co–V foils [J]. Journal of Alloys and Compounds, 2014, 615: 56–64.
- [22] MALEK GHAINI F, HAMED M J, TORKAMANY M J, SABBAGHZADEH J. Weld metal microstructural characteristics in pulsed Nd: YAG laser welding [J]. Scripta Materialia, 2007, 56(11): 955–958.
- [23] HAZRATINEZHAD M, ARAB N B M, SUFIZADEH A R, TORKAMANY M J. Mechanical and metallurgical properties of pulsed neodymium-doped yttrium aluminum garnet laser welding of dual phase steels [J]. Materials & Design, 2012, 33: 83–87.
- [24] SONG Y G, LI W S, LI L, ZHENG Y F. The influence of laser welding parameters on the microstructure and mechanical property of the as-joined NiTi alloy wires [J]. Materials Letters, 2008, 62(15): 2325–2328.
- [25] TZENG Y. Parametric analysis of the pulsed Nd: YAG laser seam-welding process [J]. Journal of Materials Processing Technology, 2000, 102: 40–47.
- [26] MONTGOMERY D C. Design and analysis of experiments [M]. New York: John Wiley & Sons, 2001.

Nd:YAG 激光微型焊接超薄 FeCo–V 磁性合金 焊接强度的优化

H. MOSTAAN¹, M. SHAMANIAN², S. HASANI³, M. SAFARI⁴, J. A. SZPUNAR⁵

1. Department of Materials and Metallurgical Engineering, Faculty of Engineering,

Arak University, Arak 38156-8-8349, Iran;

2. Department of Materials Engineering, Isfahan University of Technology, 84156-83111, Iran;

3. Department of Mining and Metallurgical Engineering, Yazd University, Yazd 89195-741, Iran;

4. Department of Mechanical Engineering, Arak University of Technology, Arak 3818141167, Iran;

5. Department of Mechanical Engineering, University of Saskatchewan, Saskatoon, SK S7N 5A9, Canada

摘要: 为了优化激光焊接 FeCo–V 合金拉伸强度, 建立数学关系, 结合工艺参数如荧光灯电流、焊接速度、脉冲时间和位置, 以预测激光束焊 FeCo–V 薄片拉伸强度。建立程序以提高焊接强度和增大产率。结果表明, 脉冲时间和焊接速度对拉伸强度影响很大, 焊接接头的拉伸强度随脉冲时间的延长而增大, 并在 2.25 ms 时达到最大。而且, 接头的拉伸强度随着焊接速度的减小而增大, 并在 125 mm/min 时达到最大。脉冲时间的延长和焊接速度的减小导致有效峰能量密度减小, 因此更耐焊。在较高的脉冲时间和较低的焊接速度时, 因为在熔合区形成了凝固微裂纹而使得焊接接头的拉伸强度增大。

关键词: Nd:YAG 激光焊接; FeCo–V 磁性合金; 响应曲面方法; 力学性能; 优化

(Edited by Xiang-qun LI)